

## Oscillatory Line-Driven Winds: The Role of Atmospheric Stratification

JOSHUA A. KEY <sup>1</sup>, DANIEL PROGA <sup>1</sup>, RANDALL DANNEN <sup>1</sup>, STERLING VIVIER <sup>1</sup> AND TIM WATERS <sup>2</sup>

<sup>1</sup>*Department of Physics & Astronomy  
University of Nevada, Las Vegas  
4505 S. Maryland Pkwy  
Las Vegas, NV, 89154-4002, USA*

<sup>2</sup>*Theoretical Division, Los Alamos National Laboratory*

Submitted to ApJ

### ABSTRACT

In a recent study, Dannen et al. surveyed a large parameter space to study the transition from efficient to inefficient line driving. They found that when the line force significantly weakens due to ionization, the winds are variable, with a characteristic frequency comparable to the Lamb cut-off frequency of a stratified atmosphere,  $\omega_c$ . In this work, we present a set of simulations and perturbation analyses that elucidate the variability source and characteristics. We found that the line force adds wave energy and amplifies perturbations with frequencies near  $\omega_c$ . This selective amplification results from the coupling between the natural tendency of velocity perturbations to grow in a stratified atmosphere and the dependence of the line force on the velocity gradient, per the Castor-Abbott-Klein line-driven wind theory. We also found that the variability stems from self-excitation that occurs in the exponential atmosphere due to the non-linearity introduced by the absolute value of the velocity gradient in the line force prescription. We conclude that self-consistently calculating ionization is insufficient for modeling the dynamics in the subsonic atmosphere. Instead future wind models should relax the Sobolev approximation, or model the radiative transfer to capture the dynamics and instabilities at the base of the wind.

*Keywords:* galaxies: active - : numerical - hydrodynamics - radiation: dynamics

### 1. INTRODUCTION

The line force can drive outflows from objects with atmospheres rich in mildly ionized metals, as these metals' bound-bound transitions significantly enhance atmospheric opacity. Such objects include accretion disk systems like cataclysmic variables (see Proga 2005, for a review) and some active galactic nuclei (AGNs; e.g., Mushotzky et al. 1972; Arav & Li 1994; Murray et al. 1995; Proga et al. 2000; Proga 2007). AGNs emit radiation over a broad energy range with a relatively large number of ionizing photons. Therefore, in some parts of their atmospheres, the ionization could be too high to sustain mildly ionized metals (Sim et al. 2010; Higginbottom et al. 2014, and references therein). To ad-

dress this concern, Dannen et al. (2020) and Dannen et al. (2024; hereafter D24) developed self-consistent wind models where hydrodynamical ('hydro' for short) calculations of the gas dynamics are coupled with ionization balance calculations (see also Dyda et al. 2017; Dannen et al. 2019). D24 surveyed the parameter space of the line force resulting from blackbody (BB) spectral energy distributions (SEDs) with temperatures ranging from  $\sim 10^4$  to  $10^6$  K and found that line driving remains efficient up to the temperature  $\approx 4 \times 10^5$  K. In addition, they ran a set of exploratory 1-D spherical wind simulations and found that the time-dependent solutions reached a steady state only in a subset of cases. D24 discovered that for the BB temperature larger than  $8 \times 10^5$  K, the line driven winds are intrinsically variable.

To explain the variability in their self-consistent simulations, D24 examined a few isothermal cases using a modified CAK method (mCAK; hereafter) introduced by Abbott (1982) to study the effect of ionization on the

line force. Specifically, D24 approximated the line force–ionization relation with a power-law scaling  $\xi^{-\delta}$ , where  $\delta$  is the parameter introduced by Abbott (1982) and  $\xi$  is the ionization parameter (see below for more details). They found that even for these simplified isothermal cases, which exclude thermal instability, the wind can be intrinsically variable or even periodic if the line force weakens significantly with increasing ionization (e.g.,  $\delta = 0.3$ ). Therefore, they attributed the variability in the solutions to the weakening of the line force instead of the thermal instability that they have observed in previous simulations with an AGN type of SED (D20).

Moreover, they found that the time-behavior of the solution depends on the so-called hydrodynamic escape parameter at the inner radius,  $r_0$ , that is,

$$\text{HEP}_0 \equiv \frac{GM(1 - \Gamma)}{r_0 a^2}, \quad (1)$$

where  $M$  is the central mass,  $a$  the sound speed, and  $\Gamma$  is the luminosity in units of the Eddington luminosity  $L_{\text{Edd}}$ . Specifically, the wind is time-independent when the atmosphere is hot or warm,  $\text{HEP}_0 < 50$ . When the wind base is cold,  $\text{HEP}_0 \gtrsim 50$ , the wind could be intrinsically variable (see Table 2 in D24).

D24 provided some clues regarding the nature of the variable solutions. Still, they did not identify the root cause of the variability. They left this task for future investigation. This paper presents our follow-up analysis and findings regarding the persistent periodic behavior of isothermal line-driven winds. We begin by noting that the main frequency of the periodic behavior is approximately the same as the Lamb cut-off frequency (Horace 1909)

$$\omega_c = \frac{a}{2H}, \quad (2)$$

characterizing an atmosphere in HSE with the density scale height,  $H = r_0/\text{HEP}_0$ .

Below, we demonstrate that the line force amplifies the low-frequency perturbations near the wind base and produces radiative-acoustic waves in the wind. The line force preferentially amplifies perturbations with frequencies below  $\omega_c$ . This selective amplification results from the coupling between the natural tendency of velocity perturbations to grow in a stratified atmosphere (see, e.g., Clarke & Carswell 2007) and the dependence of the line force on the velocity gradient, per the CAK line-driven wind theory. We also provide our current understanding of the process leading to self-excitation of perturbations that operates at the deepest layers of the atmosphere where the flow velocity is tiny and CAK line force parametrization introduces a non-linear effect.

The paper is organized as follows. In § 2, we describe our methods. In § 3, we present the results of our anal-

ysis of the hydro calculations and our solutions of the wave equation. In § 4, we discuss our results and conclude.

## 2. METHODS

To take a step forward in reducing the number of free parameters, D24 used the photoionization code XSTAR<sup>1</sup> (Kallman & Bautista 2001) to self-consistently compute the radiative heating and cooling rates and the radiation force due to spectral lines on the gas due for various SEDs. They parameterized the heating and cooling rates with gas temperature,  $T$ , and ionization parameter

$$\xi \equiv (4\pi)^2 \frac{J_X}{n_{\text{H}}}, \quad (3)$$

where  $J_X$  is the mean intensity integrated over the 0.1–1000 Ry range and  $n_{\text{H}}$  is the number density of hydrogen nucleons. D24 computed and parameterized the line force with the aforementioned ionization parameter and optical depth parameter,  $t = \sigma_e \rho \lambda_{\text{Sob}}$ , where  $\sigma_e$  is the mass scattering coefficients for free electrons and  $\lambda_{\text{Sob}} = v_{\text{th}}/|v'|$  where  $v_{\text{th}}$  is the gas thermal velocity and  $v' = \partial v / \partial r$  is the velocity gradient of the gas in the radial direction. They found that for a given mass and SED, the efficiency of line driving and the wind solution depends on three dimensionless parameters:  $\text{HEP}_0$ ,  $\Gamma$ , and  $\Xi_0$ . The latter parameter is the pressure ionization parameter defined at the wind base

$$\Xi_0 \equiv \xi_0 / (4\pi c k_B T_0). \quad (4)$$

The parameter  $\text{HEP}_0$  sets the strength of the thermal driving in the solution, while the parameters  $\Gamma$  and  $\Xi_0$  set the strength of the line driving by determining the line optical depth parameter,  $t_0$  at the wind base (see eq. B8 in D24). Typically, the number of driving lines increases with decreasing  $\Xi_0$ . However, for relatively small  $\Xi_0$ , the optical depth could become too large for the line force to operate despite the presence of many driving lines.

Most of the data analyzed in this paper come from simulations carried out by D24. However, to pin down the mechanism responsible for variability, we also performed additional simulations using the same methodology as the original ones. Therefore, we will provide only a summary of the numerical method below (for more details, refer to D24).

### 2.1. Numerical Simulations

<sup>1</sup> <https://heasarc.nasa.gov/lheasoft/xstar/xstar.html>

We use the magnetohydrodynamic code Athena++ (Stone et al. 2020) to solve the equations of hydrodynamics for 1-D spherical winds driven by a radial radiation field

$$\frac{\partial \rho}{\partial t} + \nabla \cdot (\rho \mathbf{v}) = 0, \quad (5)$$

$$\frac{\partial (\rho \mathbf{v})}{\partial t} + \nabla \cdot (\rho \mathbf{v} \mathbf{v} + \mathbf{P}) = -\rho \nabla \Phi_{\text{eff}} + \mathbf{g}_l, \quad (6)$$

and

$$\frac{\partial E}{\partial t} + \nabla \cdot [(E + p)\mathbf{v}] = -\rho \mathbf{v} \cdot \nabla \Phi_{\text{eff}} + \mathbf{v} \cdot \mathbf{g}_l, \quad (7)$$

where  $\rho$ ,  $\mathbf{P}$ ,  $\mathbf{v}$ , and  $E$  are the gas density, pressure, velocity, and energy density, respectively. In addition,  $\mathbf{P} = p\mathbf{I}$  is the pressure tensor where  $p$  is the scalar pressure and  $\mathbf{I}$  is the unit tensor. Moreover,  $E = \rho \mathcal{E} + 1/2 \rho |\mathbf{v}|^2$  is the energy density while  $\Phi_{\text{eff}} = -GM(1 - \Gamma)/r$  is the effective gravitational potential.

We compute the line force,  $\mathbf{g}_l$  using the method introduced by CAK

$$\mathbf{g}_l = M(t, \xi) g_{\text{es}} \hat{\mathbf{r}}, \quad (8)$$

where  $M(t, \xi)$  is the force multiplier and  $g_{\text{es}}$  is the radiation force due to electron scattering. We approximate the force multiplier dependence on the optical depth,  $t$ , and ionization parameter,  $\xi$ , using power laws:

$$M(t, \xi) = k_0 (\xi_0 / \xi)^\delta (t)^{-\alpha}, \quad (9)$$

and assume  $M = 10 M_\odot$  and  $\Gamma = 0.2$ . We also compute a reference radius  $r_0 = [GM(1 - \Gamma)] \text{HEP}_0^{-1} a^{-2}$ . For the original calculations, the inner radius of the computational domain is  $r_{\text{in}} = r_0$ . For additional simulations, we explored cases where  $r_{\text{in}} < r_0$ , see §3.4. In addition, we assume the adiabatic index  $\gamma = 1.0001$ ,  $T = 9.18 \times 10^4$  K, and  $\xi_0 = 80 \text{ erg cm s}^{-1}$ . In these models, we set the multiplier parameters  $k = 0.0076$  and  $\alpha = 0.742$ . We examine wind solutions for various  $\delta$  values ranging from 0 to 0.4 to investigate the wind solution's dependence on ionization.

We apply the same initial conditions as D24. We also run the simulations in two stages as in D24: (i) we allow the solution to evolve with outflow boundary conditions for 10 to 30 % of the total runtime and (ii) we pause the simulation, modify the outer boundary condition to constant gradients, and continue the simulation for the remaining runtime.

## 2.2. Data Decomposition and Theoretical Description

We followed a standard procedure to study the periodic nature of the solutions. We decomposed a given

wind quantity,  $q(t)$ , into a time-independent background value,  $\langle q \rangle$ , and time-dependent (Eulerian) perturbation,  $q_1(t)$ . To compute  $\langle q \rangle$ , we averaged  $q$  over approximately a hundred oscillation periods using the data from the end of the simulation, when the solution evolved far from the initial transient. Then, we subtracted that average from the time-dependent quantities to isolate the oscillatory perturbations, i.e.,  $q(t) - \langle q \rangle = q_1(t)$ . To simplify notation, we will omit the brackets  $\langle q \rangle$  throughout the paper and refer to the time-averaged quantities simply as  $q$ . To avoid confusion, we write the time-dependent quantity as  $q(t)$  when necessary.

In the top panel of Fig. 1, we show the time-averaged radial profiles of density, velocity, and the velocity gradient for the periodic  $\delta = 0.3$  solution. These time-averaged profiles do not show any unusual features and are similar to the steady-state solutions. The middle panel illustrates  $\rho(t_1)$ ,  $v(t_1)$ ,  $v'(t_1)$  profiles at a particular time,  $t_1$  while the bottom panel shows the Eulerian perturbations:  $\rho_1(t_1)$ ,  $v_1(t_1)$ , and  $v'_1(t_1)$ .

In Fig. 2, we show the results of a Fourier analysis examining the temporal properties of the perturbations. In the top panel, we present the temporal signal at  $r = 1.005 r_0$  and  $r = 1.196 r_0$ , blue and red curves, respectively. We indicated these two locations with downward-pointing arrows in the bottom panel of Fig. 1. In the bottom panel of Fig. 2, we present the frequency power spectrum, which shows a clear preferential amplification of the fundamental mode at  $\omega = 0.628 \omega_c$ . We will revisit these two figures in the next section.

To quantify the wave behavior seen in the periodic solutions, we measure the wave energy and its evolution and examine the solutions of a mass-flux wave equation. In Appendix A.1, we derive the wave energy conservation equation

$$\begin{aligned} \frac{\partial E_w}{\partial t} + \frac{1}{r^2} \frac{\partial (r^2 p_1 v_1)}{\partial r} = \\ -\rho v_1 \frac{\partial (v v_1)}{\partial r} - \frac{\rho_1}{\rho} \frac{1}{r^2} \frac{\partial (r^2 p_1 v)}{\partial r} + \rho v_1 g_{l,1}, \end{aligned} \quad (10)$$

where  $E_w$  is the specific acoustic energy defined as the sum of the potential energy component,  $PE_w$  and the kinetic energy component,  $KE_w$ ,

$$E_w \equiv PE_w + KE_w = \frac{1}{2} \frac{p_1^2}{\rho a^2} + \frac{1}{2} \rho v_1^2. \quad (11)$$

The perturbed line force,  $g_{l,1}$ , can be expressed as

$$g_{l,1} = 2v_a \left[ \left( \frac{\delta}{\alpha} - 1 \right) \frac{\rho_1}{\rho} v' + v'_1 \right], \quad (12)$$

where  $v_a$  is the Abbott speed that depends on the ratio between the background line force and the velocity

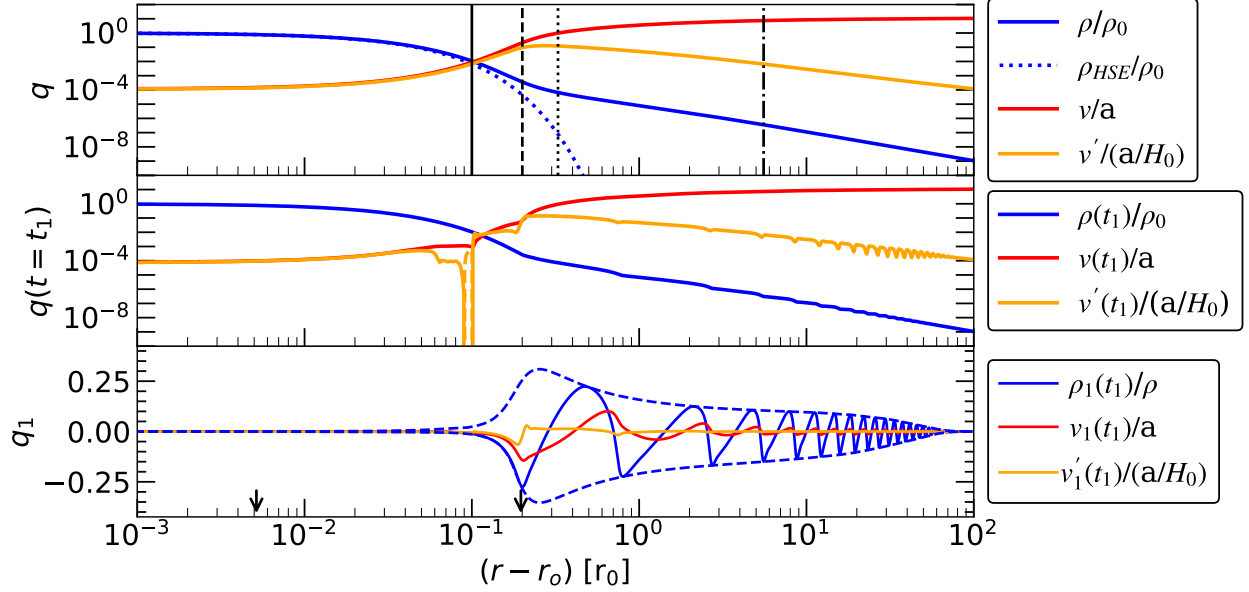


**Figure 1.** Radial profiles of various wind properties of the  $\delta = 0.3$  periodic solution. We list the specific quantities plotted here in the legends and below. The top panel shows the time-averaged profiles, which closely resemble those for the steady-state solutions. The black solid and dashed vertical lines mark the outer radius of the unsteady and unstable regions, respectively (see § 3.4 and 3.2 for more detail). The vertical dotted and dash-dotted lines indicate the sonic and critical points, respectively. The middle panel shows an example of time-dependent radial profiles from the simulation at a particular instance  $t_1 = 1.59 P_c$ . We marked this time in Fig. 2 and used the data for this to generate the left panels of Fig. 5. The bottom panel shows the perturbed quantities obtained by subtracting the data in the middle panel and the time-averaged profiles in the top panel. The two dashed curves represent the envelopes of the perturbed density. In the bottom panel, the small vertical arrows at  $r = 1.005 r_0$  and  $1.196 r_0$  mark the positions we use in the Fourier analysis results presented in Fig. 2.

gradient:

$$v_a \equiv \frac{1}{2} g'_l = \frac{1}{2} \frac{\partial g_l}{\partial (v')} = \frac{\alpha g_l}{2 v'}. \quad (13)$$

The right-hand side (RHS) of eq. 10 contains the sink and source terms that either add or remove energy from the acoustic wave. In a static, homogeneous fluid, these terms equal zero and the flux of energy density entering or leaving a location  $r$  drives the time rate of change of  $E_w$ .

In Appendix A.2, we derived the mass flux wave equation for an isothermal mCAK line-driven wind:

$$\begin{aligned} \frac{\partial^2 f_1}{\partial t^2} + 2v_{\text{eff}} \frac{\partial^2 f_1}{\partial r \partial t} + (v_{\text{eff}}^2 - a_{\text{eff}}^2) \frac{\partial^2 f_1}{\partial r^2} = \\ + \frac{a_{\text{eff}}^2 - 3v_{\text{eff}}^2}{\lambda_v} \frac{\partial f_1}{\partial r} + \frac{2v_a (v_a - v(\frac{\delta}{\alpha}))}{\lambda_v} \frac{\partial f_1}{\partial r} \\ - \frac{2v_{\text{eff}}}{\lambda_v} \frac{\partial f_1}{\partial t}, \end{aligned} \quad (14)$$

where  $v_{\text{eff}} = v - v_a$ ,  $a_{\text{eff}}^2 = a^2 + v_a^2$ , and  $\lambda_v = v/v'$ , and the mass flux perturbation defined as

$$f_1 \equiv f \left( \frac{\rho_1}{\rho} + \frac{v_1}{v} \right). \quad (15)$$

The mass flux  $f = r^2 \rho v$  is constant. Eq. 14 reduces to the Abbott wave equation when one neglects gravity, stratification, and divergence (see eq. 42 in Abbott 1980). We also note that when  $v_a = 0$ , eq. 14 reduces to the isothermal acoustic wave equation (see eq. 6 in Petterson et al. 1980).

### 3. RESULTS

As mentioned in § 1, we identified an instability that amplifies radiative-acoustic waves in a small region inside a strongly stratified, nearly hydrostatic atmosphere. We found that the subsonic highly stratified part of each periodic solution has two distinct regions: (i) unsteady region where perturbations are self-excited and (ii) unstable region where perturbations are amplified. In the top panel of Fig. 1, we use the vertical solid and dashed lines to mark the outer radius of these two regions (we also mark the sonic and critical points using the dotted and dash-dotted lines).

To ascertain the source of the instability, we begin in § 3.1 by discussing how the time-averaged flow properties depend on  $\delta$ . In § 3.2 we discuss the flow properties responsible for the instability and how they lead to a wave amplitude that grows beyond that predicted by

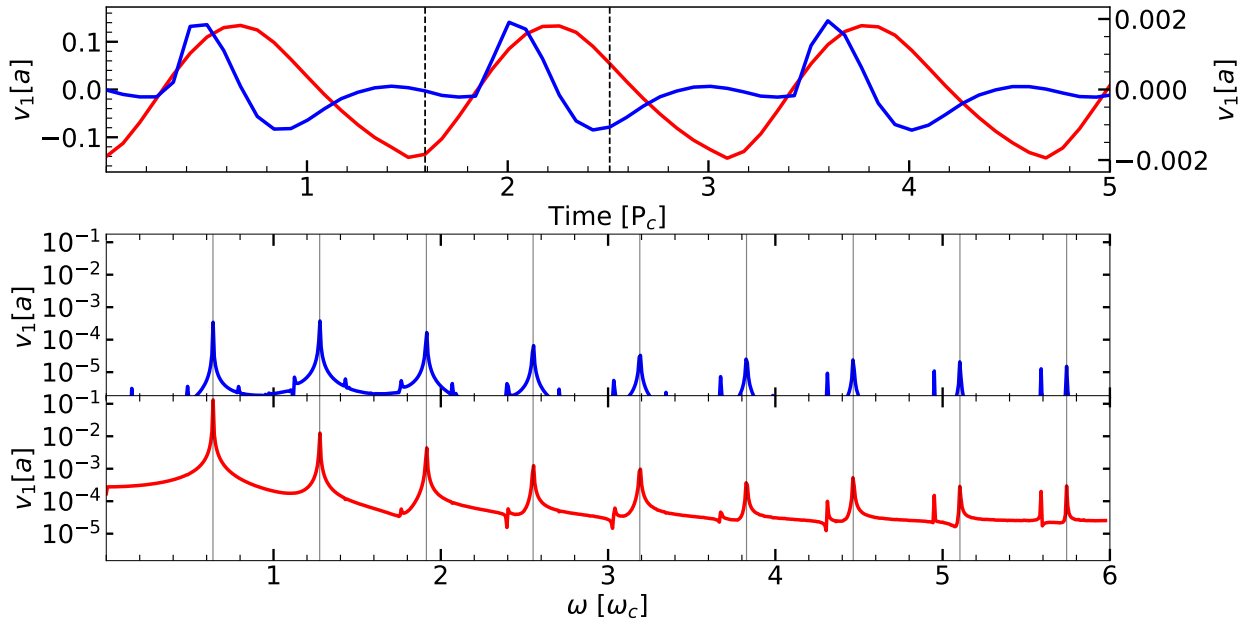


**Figure 2.** Time variability of the wind properties. The top panel shows examples of the velocity perturbation as a function of time at the two radii marked with the small arrows in the bottom panel of Fig. 1 (i.e., at  $r = 1.005 r_0$  and  $1.196 r_0$ , blue and red curves, respectively). The dashed vertical lines in the top panel denote times  $t_1$  and  $t_2$ , where  $t_1$  is the time snapshot used in the middle and bottom panels of Fig. 1 and in the left panels in Fig. 5, while  $t_2$  is the snapshot used in the right panels of Fig. 5. The middle and bottom panel shows the Fourier transform of the temporal signal at  $r = 1.005 r_0$  and  $1.196 r_0$ , respectively. The vertical gray lines in this pair of panels denote integer multiples of the lowest fundamental frequency,  $\omega = 0.628 \omega_c$ . The lines demonstrate that the higher frequencies are higher orders of the fundamental frequency. The middle panel shows that in the unsteady region, the oscillation amplitudes of the three lowest fundamental frequencies are similar to each other and greater than the amplitude of higher-order frequencies. The bottom panel shows that the perturbation amplitudes grow rapidly as the perturbations move through the unstable region while maintaining the same frequency structure. Although all frequencies experience growth, the lowest fundamental frequency grows at least an order of magnitude more than the others.

conserving wave energy flux in a stratified atmosphere. In § 3.3 and § 3.4, we return to our discussion of the amplification and source of the perturbation. Unless stated otherwise, we describe the behavior of the solution for  $\delta = 0.3$ . The qualitative features of the time-dependent behavior observed in the  $\delta = 0.3$  solution are similar to those found across periodic solutions within the range of  $\delta$  from 0.23 to 0.4.

### 3.1. *mCAK Critical Point and Abbott Speed*

The emergence of periodic oscillations in the wind solutions for  $\delta > 0$  are related to changes in the characteristics of the background flow, specifically the magnitude of the velocity and velocity gradient near the inner boundary. Qualitatively this makes sense in the context of the analogy from Owocki (2020). In the line driven winds of OB stars, the line force drives material away from the star creating a suction that allows the material from the hydrostatic region to expand upward through the sonic point. By increasing the ionization dependence

via  $\delta$  and weakening the line force, the suction effect lessens, leaving the material in an increasingly hydrostatic state (reduced velocity and velocity gradient).

In early work, researchers modeled line force weakening with  $\delta$  parameters ranging from 0-0.16 and found agreement with predicted and observed mass loss rates of OB stars (Lamers & Cassinelli 1999). More recently, Curé et al. (2011) studied line driven winds for a large range of  $\delta$  (0 – 0.42) and found the emergence of a new type of stationary solution, the  $\delta$ -slow solution. The  $\delta$ -slow solutions exhibit slower terminal velocities and mass loss rates around a 100 times lower than the fast wind solutions, in agreement with observations of Type-A supergiants. Additionally, Curé et al. (2011) found no slow wind solutions in the range  $\delta = 0.23 - 0.30$ . Larger values of  $\delta$  are typically unrealistic for OB stars, however for hydrogen winds Puls, J. et al. (2000) showed that  $\delta \sim 0.3$ , and Kudritzki (2002) demonstrated that low metallicities significantly increases the number of ionizing photons in the wind. In the context of AGN



and XRBs, [Dannen et al. \(2024\)](#) calculated  $k$ ,  $\alpha$ , and  $\delta$  and found that  $\delta$  can approach values of  $\alpha$  in line driven winds.

To investigate evolution of background properties specific to our line driving parameters  $\xi_0 = 80 \text{ erg cm s}^{-1}$ ,  $k = 0.0076$  and  $\alpha = 0.742$ , we follow [CAK](#)'s mathematical analysis of the steady-state momentum equation expressed as

$$F(r, v, v') \equiv 1 + w' + \frac{1}{2\text{HEP}_0} \frac{w'}{w} + \frac{2}{\text{HEP}_0} \frac{r}{r_0} - Ch(|w'|)^\alpha = 0, \quad (16)$$

where  $w = v^2/[(1-\Gamma)v_{esc}^2]$ ,  $w' = \frac{\partial w}{\partial n}$ ,  $n = 1 - r_0/r$ , and  $h$  is a dimensionless correction factor that could related to the finite disk correction or ionization effects. In our models, this factor is purely due to the latter, hence  $h = (\xi_0/\xi)^\delta$ . Using the function  $F(r, v, v')$  and time-averaged quantities, we compute the regularity equation,

$$F_r \equiv \frac{\partial F}{\partial v'}, \quad (17)$$

and the singularity equation,

$$F_s \equiv \frac{\partial F}{\partial r} + v' \frac{\partial F}{\partial v}. \quad (18)$$

We plot these two functions using red and blue curves in the top panel of Fig. 3. The critical point of the wind solution is where both functions are equal to zero, and it occurs at  $r_c = 6.55 r_0$  (see the vertical black dashed line in the top panel of Fig. 3; we also marked this point with the vertical dashed-dotted line in the top panel of Fig. 1). Additionally, we derived an explicit relation for how  $r_c$  depends on  $\delta$ :

$$1 - \frac{\delta}{2\alpha} - \left( \frac{v_c}{r_c v'_c} \right)^2 \left( 1 - \frac{\delta}{2\alpha} \left( \frac{r_c v'_c}{a} \right)^2 \right) = 0. \quad (19)$$

This equation reduces to the classical CAK critical point condition,  $v_c/r_c = v'_c$ , for  $\delta = 0$ . In our subsequent literature search, we found work by [Curé & Araya \(2023\)](#) and that their critical function (eq. 57) simplifies to our eq. 19 when one neglects the effects of the finite disk correction factor and rotation.

The  $v_c/r_c = v'_c$  condition only implies a slight outward shift in the critical point due to the weakening of the line force via  $\delta$ . By including the critical point's explicit dependence on  $\delta$ , i.e., using eq. 19, we show that the critical point shifts significantly. In the  $\delta = 0$  solution, the critical point is at  $r_c = 1.93 r_0$ , while for the  $\delta = 0.3$  solution, the critical point is farther out by a factor more than 3, i.e.,  $r_c = 6.55 r_0$ . We verified

eq. 19 with calculations of eq. 17 and eq. 18 (see the top panel of Fig. 3).

Unlike  $r_c$ , we found that  $v_c$  does not strongly depend on  $\delta$ . Consequently, the wind acceleration decreases with increasing  $\delta$ . This trend also influences another characteristic of line-driven winds: the Abbott speed (see the bottom panel of Fig. 3.) We can describe the increase of  $v_a$  with  $\delta$  by the following scaling:

$$v_a \propto \frac{v^{-\delta} v'^\alpha}{v' \rho^\alpha} \propto \frac{v'^{\alpha-\delta-1}}{\rho^\alpha} \quad (20)$$

The density dependence,  $\rho^{-\alpha}$ , arises from the line-force dependence of the density through the optical depth. In HSE, gas density does not appreciably depend on  $\delta$ . Therefore, the change in  $v_a$  induced by modifying  $\delta$  comes only through  $v$  and  $v'$ . The velocity dependence,  $v^{-\delta}$ , stems from the ionization dependence and the velocity gradient dependence,  $v'^\alpha$ , comes from the optical depth in eq. 8. At small radii, as  $\rho$  decreases exponentially,  $v$  increases exponentially, and  $v \propto v'$  (compare the red and orange curves in the top and middle panels of Fig. 1), leading the final expression on the RHS of eq. 20. The net result is almost an order of magnitude increase in  $v_a$  for nearly two orders of magnitude decrease in  $v$  and  $v'$ . Thus, for the  $\delta = 0.3$  solution, the stratified region increasingly becomes hydrostatic whereas  $v_{\text{eff}}$  becomes an order of magnitude more negative across a region five times larger than that of the  $\delta = 0$  solution (see the dashed curves in the bottom panel of Fig. 3). Generally, as  $\delta$  increases, the outer radius of the negative  $v_{\text{eff}}$  region increases. In a purely Parker wind,  $v_{\text{eff}}$  would always be positive, so we attribute the extension of this negative region to the growth of radiative acoustic waves. We provide more support for this below.

### 3.2. Wave Energy

We use eq. 10 and simulation data to compute the time-averaged wave energy rate and the corresponding source/sink terms. In Fig. 4, the solid curve shows the average wave energy rate,  $\langle \frac{dE_w}{dt} \rangle$ , i.e., the LHS of eq. 10. In the unsteady region, the rate is positive but relatively small at the smallest radii. However, the rate dramatically increases farther downstream in the unstable region and reaches a maximum at  $r \simeq 1.17 r_0$ . This increase directly corresponds to the sharp increase in the perturbation amplitudes, as shown in the bottom panel of Fig. 1. Even farther downstream, the rate decreases and becomes negative at  $r \simeq 1.85 r_0$ . The dashed curve represents the source and sink terms on the RHS of eq. 10. Both curves agree, confirming the expectation from the linear analysis that the source/sink terms directly drive the changes in the wave energy rate

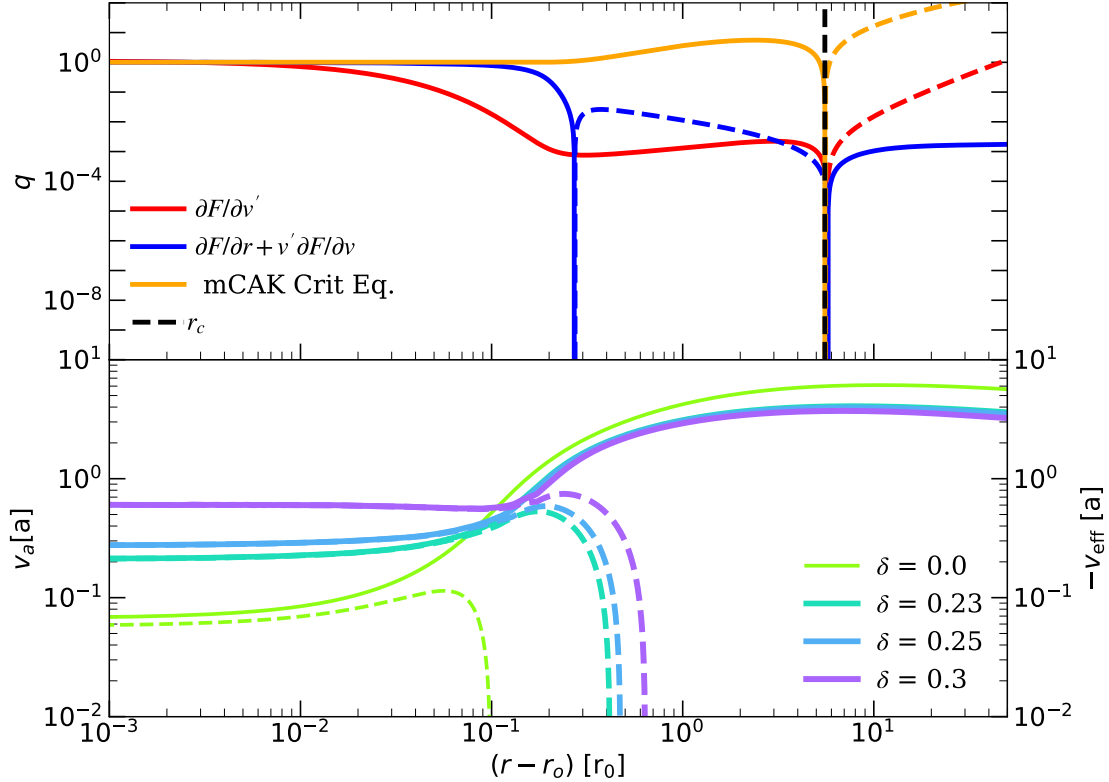


**Figure 3.** Comparison of radial profiles of wind properties. The top panel shows the location of the critical point,  $r_c$ , for the  $\delta = 0.3$  solution. The vertical dashed black line marks the location where the LHS of eq. 19 (orange curve) equals zero. We confirm that at  $r_c$  as determined by eq. 19 coincides with the radius where the regularity and singularity conditions are satisfied, i.e., where both eq. 17 (red) and eq. 18 (blue) equals zero. All curves in the top plot are normalized to equal one at  $r = r_0$ . The bottom panel illustrates how the weakening of the line force (i.e., an increase in  $\delta$ ) changes the wind properties. The solid curves correspond to the Abbott speed,  $v_a$  (refer to the ordinate axis of the left and see eq. 13 for the definition of  $v_a$ ) while the dashed curves correspond to the negative value of the effective velocity,  $v_{\text{eff}} = v - v_a$  (refer to the ordinate axis of the right). The effect of increasing  $\delta$  is the strongest at the smallest radii, where the stratification is the highest. The increase/decrease of the Abbott speed/flow velocity with  $\delta$  results in the increase of the size of the inner region where  $v_{\text{eff}} < 0$ . This size is five times larger, while  $v_a$  is nearly an order of magnitude greater for  $\delta = 0.3$  compared to  $\delta = 0$ . Note that for small radii and high  $\delta$ , the solid and dashed curves overlap because  $v/v_a \ll 1$  and  $-v_{\text{eff}} \simeq v_a$ .

of change. The dash-dotted curve shows only the line driving term on the RHS of eq. 10,  $\langle \rho v_1 g_{l,1} \rangle$ . We found that this term is responsible for depositing energy into the wave at small radii. It is positive up to the radius of  $1.2 r_0$ , which we defined as the outer radius of the unstable region.

Based on scaling relations of a linear pressure wave, we wouldn't expect a positive contribution from  $\langle \rho v_1 g_{l,1} \rangle$ . We can express the power produced by the perturbed line force in terms of  $\rho_1$  and  $v_1$  as

$$\rho v_1 g_{l,1} = 2v_a \left[ \left( \frac{\delta}{\alpha} - 1 \right) \rho_1 v_1 v' + \rho v_1 v'_1 \right]. \quad (21)$$

For a linear acoustic perturbation  $\rho_1 \propto v_1$  whereas  $i(2\pi/\lambda)v_1 \propto v'_1$ . Therefore, the  $\rho_1 v_1$  contribution would indicate energy removal and  $v_1 v'_1$  would contribute no net effect. Thus, the net contribution of all three terms on the RHS of eq. 10 should be negative when considering a local oscillatory perturbation (for more detail, see Appendix A.3 and Key et al., submitted).

The clue to the positive value of  $\langle \rho v_1 g_{l,1} \rangle$  comes from Fig. 1 which shows  $v_1$  is nearly proportional to  $v'_1$  in the stratified region. In this region, the WKB approximation does not apply because the spatial component of the phase,  $\phi$ , changes over a similar scale as the perturbation.

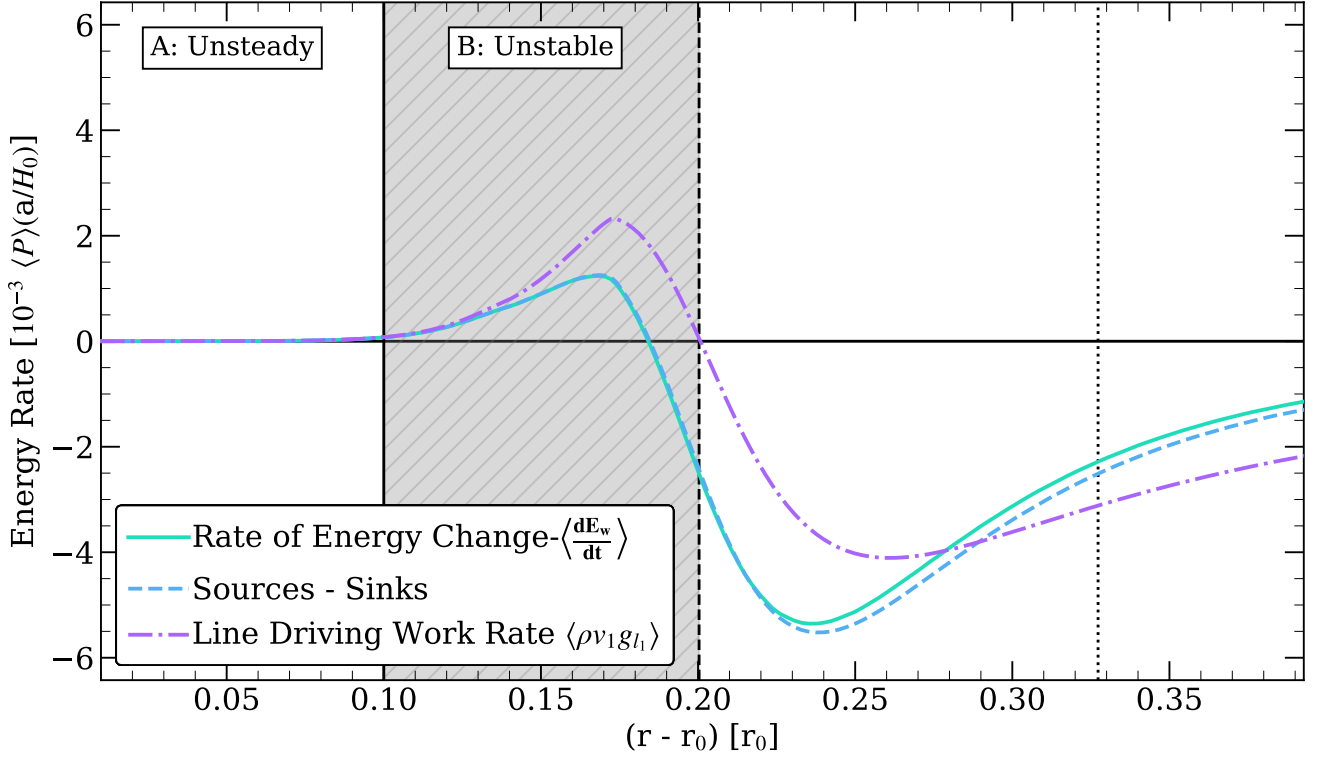


**Figure 4.** Radial profiles of the time-averaged terms in the wave energy equation, eq. 10 (see the legend in the bottom left corner). The dashed vertical line marks the radius where the line force’s work rate equals zero. We use this radius to delineate the boundary between the highly stratified atmosphere and the launched wind. We refer to the former and latter as unstable and transonic regions. The solid black line, determined empirically (see § 3.4), marks the boundary between the intrinsically time-dependent flow and the unstable region (shaded in gray). We refer to the intrinsically time-dependent region as the ‘unsteady’ region. In this region, self-excitation generates waves that grow in the unstable region. The dotted line marks the sonic point. Note that all relevant activity is in the subsonic, almost static, region.

bation amplitude,  $|q_1|$ , i.e.,

$$\left| \frac{d\phi(r)}{dr} \right| \approx \frac{|q'_1|}{|q_1|}. \quad (22)$$

Obtaining analytical results in this regime is challenging and beyond the scope of this work.

In the simplified case of an acoustic wave in a hydrostatic stratified atmosphere, one can show that  $v_1 \propto \exp(z/2H) \exp[i(2\pi/\lambda)z - \omega t]$  and  $\lambda = \text{constant}$ , therefore  $\langle v_1 v'_1 \rangle \neq 0$ . We note that in our simulations, the line force ceases to perform positive work at the end of the stratified region. This transition is ubiquitous across the periodic simulations with  $0.23 \leq \delta \leq 0.4$ , indicating the exponentially stratified atmosphere is critical for wave energy growth. We elaborate on this point by considering the wave equation, eq. 14.

### 3.3. Instability

All terms on the RHS of eq. 14 depend on the fluid stratification as they contain  $\lambda_v$  in the denominator.

Thus,  $\lambda_v$  sets the frequencies characterizing the stratification and line driving: (i) the acoustic cut-off frequency,  $\omega_c = a/2\lambda_v$  and (ii) the line-driving frequency  $\omega_{\text{eff}} \equiv -v_{\text{eff}}/\lambda_v \simeq v_a/\lambda_v$ . Because  $v$  is nearly zero ( $v/a < 10^{-1}$ ) and  $v_{\text{eff}}$ ,  $v_a$  and  $a_{\text{eff}}$  are nearly constant in much of the unstable region, we can simplify eq. 14 to

$$\frac{\partial^2 f_1}{\partial t^2} - 2v_a \frac{\partial^2 f_1}{\partial r \partial t} - a^2 \frac{\partial^2 f_1}{\partial r^2} = 2\omega_c a \frac{\partial f_1}{\partial r} + 2\omega_{\text{eff}} \frac{\partial f_1}{\partial t}, \quad (23)$$

In our simulation,  $v_a \simeq 0.6 a$ , so  $a_{\text{eff}} \simeq 1.2 a$  and  $\omega_{\text{eff}} \simeq 1.2 \omega_c$ . To compare the characteristic length scale of the line driving, we recast eq. 23 using the normal variables  $x = r - (v_{\text{eff}} + a_{\text{eff}})t$  and  $y = r + (-v_{\text{eff}} + a_{\text{eff}})t$ :

$$-4 \frac{\partial^2 f_1}{\partial x \partial y} = \frac{A_1 + A_2}{\lambda_v} \frac{\partial f_1}{\partial x} + \frac{A_1 - A_2}{\lambda_v} \frac{\partial f_1}{\partial y}, \quad (24)$$



where

$$A_1 \approx 1 + \frac{v_a^2}{a_{\text{eff}}^2}, \quad (25)$$

and

$$A_2 \approx 2 \frac{v_a}{a_{\text{eff}}}. \quad (26)$$

For  $\delta = 0.3$ ,  $(A_1 + A_2) \simeq 9/4$  and  $(A_1 - A_2) \simeq 1/4$ . Without line driving,  $(A_1 + A_2) = 1$  and  $(A_1 - A_2) = 1$ . Given the factors  $A_1$  and  $A_2$  are comparable, we expect the line driving and stratification effects to operate on a similar length scale. We note that the line force not only breaks the symmetry in the propagation speeds of the acoustic modes but also breaks the symmetry between the characteristic lengths for the inward and outward modes in a stratified atmosphere.

Based on the similar characteristic lengths and frequencies between the stratified acoustic behavior and the line force, we expect qualitatively different behavior for frequencies above  $\omega_c$  and below  $\omega_c$ , which we see in Fig. 2. We note that  $\omega_{\text{eff}}$  will approach zero and become negative as  $v$  approaches and exceeds  $v_a$ , occurring outside the exponentially stratified region near  $r \simeq 1.6 r_0$ . Crucially,  $\omega_c$  and  $\omega_{\text{eff}}$  will both approach zero as  $\lambda_v$  increases, reinforcing the conclusion of § 3.2 that the exponentially stratified atmosphere is critical to wave energy growth for the periodic simulations.

To gain further insight into how line driving increases  $\rho_1$  and  $v_1$ , we return to the general case of 14. We numerically solve eq. 14 for the dominant frequency observed in the simulations.

For completeness, we briefly describe our method below. We substitute  $f_1 = g(r)h(t)$  where  $h(t) = \exp[-i\omega t]$  into eq. 14, decomposing the wave equation into the complex second-order ODE:

$$\begin{aligned} & \left( \omega^2 + \frac{2i\omega v_{\text{eff}}}{\lambda_v} \right) g(r) \\ & + \left( \frac{a_{\text{eff}}^2 + 2v_a(v_a - v_{\frac{\delta}{\alpha}}) - 3v_{\text{eff}}^2}{\lambda_v} + 2i\omega v_{\text{eff}} \right) g'(r) \\ & + (a_{\text{eff}}^2 - v_{\text{eff}}^2) g''(r) = 0. \end{aligned} \quad (27)$$

We force a continuous, purely real oscillation frequency at the inner radius using the above substitution. Physically, the continuous oscillation would be analogous to having a driver at the wind base sinusoidally perturbing the wind at a specific amplitude. The imposed real frequency forces amplitude changes to depend on the imaginary components of the spatial solution,  $g(r)$ . We solved eq. 27 by splitting the 2nd-order ODE into a system of first-order ODEs, using a Runge-Kutta solver. We applied the Neumann and Dirichlet boundary condition for an outward propagating homogenous eigenmode, and updated the coefficients of the ODE at each

grid point using the background quantities supplied by the time-average flow properties. We apply a perturbation amplitude of  $2.7 \times 10^{-3}$  for both  $\rho_1/\rho$ , and  $v_1/a$  at the wind base, and set the frequency to  $\omega = 0.628 \omega_c$ . With the solution of  $f_1$ , we extract  $\rho_1$  and  $v_1$  by using eq. A1 and eq. 15 to obtain the complete acoustic wave behavior of the system.

We present the results of our calculations in Fig. 5. In the left column, we show a time snapshot of the simulation results used in Fig. 1 and the corresponding time snapshot from the linearized solution. In this snapshot, the linearized solution exhibits similar amplitude and phase behavior for  $\rho_1/\rho$  and  $v_1/a$  compared to the simulation results. Additionally, the linearized solution shows similar energy growth and distribution among kinetic and potential wave energy. In the right column, we show that in the time-dependent simulation, there is a time during the periodic cycle when eq. 14 does not adequately capture the periodic behavior. Specifically, we find a snapshot containing a kink in the unsteady flow region in the simulation results. The kink is a discontinuous change in the slope of  $v_1$  corresponding to a discontinuous jump in  $v'_1$ . We determined that the kink is caused by the absolute value of  $v'$  in the force multiplier prescription. We will discuss the kink and its significance in § 3.4.

Overall, we found that oscillatory behavior originates in the unsteady region. The solution continuously oscillates in this region, injecting fluctuations into the rest of the domain. As fluctuations propagate, they evolve in shape and amplitude, becoming Abbott waves that can be, to some degree, captured by eq. 14.

Three factors limit the spatial and temporal similarity between the linearized solution and the simulation. First, the wave in the simulation contains multiple frequencies (shown in Fig. 2). Second, the simulation results include the second-order effects neglected in the linearized solution. Lastly, the linearized solution is not a pure outward propagating wave. At frequencies comparable to  $\omega_c$ , there is coupling between the homogeneous outward and inward propagating eigenmodes of acoustic waves in an isothermal wind (Grappin et al. 1997). Therefore, using the homogeneous outward propagating boundary conditions does not yield a pure outward propagating wave.

In the linearized solution, we found that the energy grows by a factor of  $\sim 256$  from the inner boundary to the end of the unstable region. This growth factor indicates an average growth scale length  $\sim 1.8 \times \lambda_v$ . We also found that this behavior directly results from the dependence of the line force on  $v'$ .

We performed wave solution calculations for different model parameters, including a case where we set  $\delta = \alpha$ . In this case, the  $\rho_1$  contribution to the line force in the linearized solution equals zero (see eq. 12). The remaining terms in the wave behavior are due to the perturbed pressure and velocity gradient in the perturbed line force. We found that the  $\delta = \alpha$  solution is qualitatively similar to the solution in Fig. 5 but has a slightly higher energy maximum and a shallower energy drop-off as the wave propagates outwards. This difference in behavior indicates that the  $\rho_1$  term removes energy from the wave via the line force. It is also consistent with the expected behavior discussed in § 3.2: the  $\langle \rho_1 v_1 \rangle$  term leads to the energy removal.

We conclude that the positive energy contribution from the line force must be from the term  $\langle v_1 v_1' \rangle > 0$  and a non-WKB behavior. In an exponentially stratified atmosphere, velocity perturbation amplitudes increase by conserving wave energy flux (Clarke & Carswell 2007). The increase induces steeper gradients, amplifying the line force and, subsequently, the wave. The feedback between the two effects continues until the specific energy sink rate from spherical divergence, wave-flow interaction, and the density contribution to the line-driving perturbation becomes significant.

### 3.4. Self-Excitation

As mentioned in § 3.3, the periodic time-dependent simulations show the reappearance of a distinctive kink in  $v_1$  in the innermost part of the flow that we call the unsteady region ( $r < 1.1 r_0$  and  $v < 0.01 a$ ). The kink emerges when the line force cannot steadily accelerate the outflow. This situation can arise when the mass flux of the wind is larger than the line force can support. Thus, the outflow must slow down and potentially turn into an inflow (e.g., Owocki 2018). The transition from an accelerating to a decelerating solution happens discontinuously due to the  $|v'|$  dependence. The transition comes from a mismatch between the mass flux and the line force caused either by weakening of the line force downstream or an increased mass flux. We found that the flow is most prone to such a mismatch at its base, where it is the slowest.

Because the absolute value is a non-linear operation, linear analysis does not capture the kink behavior. We see the departure from linear analysis in Fig. 5, occurring mainly at  $r < 1.1 r_0$ . Additionally, we noticed that the early evolution of a solution that reaches a steady state is very similar to that of a persistently periodic solution. Namely, during an initial transient of a steady-state solution, the innermost region produces self-excited perturbations. The main difference is that

the perturbations gradually diminish in the steady-state solutions. For the periodic solutions, the evolution appeared as if it could reach a steady state if not for some process operating in the hydrostatic stratified region.

Motivated by both factors, we reran the simulation with  $r_{in}$  set to  $1.1 r_0$  instead of  $1 r_0$ . For this case, the initial phase with perturbations was short-lived and the solution quickly reached a steady state. Thus, by moving the simulation's lower boundary outward, we excluded the unsteady region from the domain, preventing oscillations from being injected into the unstable region.

We ran additional simulations for various  $r_{in}$  and found that the solutions are periodic for  $r_{in} < 1.1 r_0$ . The periodic solutions' time-averaged density and velocity profiles are practically identical to the profiles of the corresponding steady solution obtained by moving the lower boundary outward.

We stress that we empirically determined the transition point at  $r = 1.1 r_0$  between the unsteady region where perturbations are self-excited and the unstable region where the perturbations grow. We have not yet identified any clear feature in the time-averaged solution that could be used to distinguish the two regions. For example, the time-averaged radial profiles presented in Figs. 1 and 3 do not show any qualitative changes around the transition point.

We conjecture that for the self-excitation process to operate, the lower boundary of the flow solution needs to be well inside the region that is almost in HSE, i.e., where the flow velocity and net force are nearly zero. In the HSE region, the thermal gas pressure almost exclusively balances gravity, while the line force primarily acts as a perturber. The weak line force minutely assists the thermal pressure in overcoming gravity but periodically fails as the flow becomes overloaded. The repetitive failure produces fluctuations that develop features characteristic of acoustic waves as they gain energy from the line force.

## 4. SUMMARY AND DISCUSSION

We investigated the persistent periodic behavior of isothermal line-driven wind solutions found by D24. We identified two distinct regions in the HSE portion of the atmosphere: (i) unsteady region where perturbations are self-excited and (ii) unstable region where perturbations are amplified. The unsteady region appears to self-excite perturbations, with the fundamental frequency close to the atmosphere's natural frequency, i.e., the Lamb cut-off frequency, see eq. 2. The self-excitation occurs where the time-averaged Mach number is very small (e.g.,  $v/a < 10^{-2}$  for the  $\delta = 0.3$  case). We attribute the self-excitation to a mismatch between the

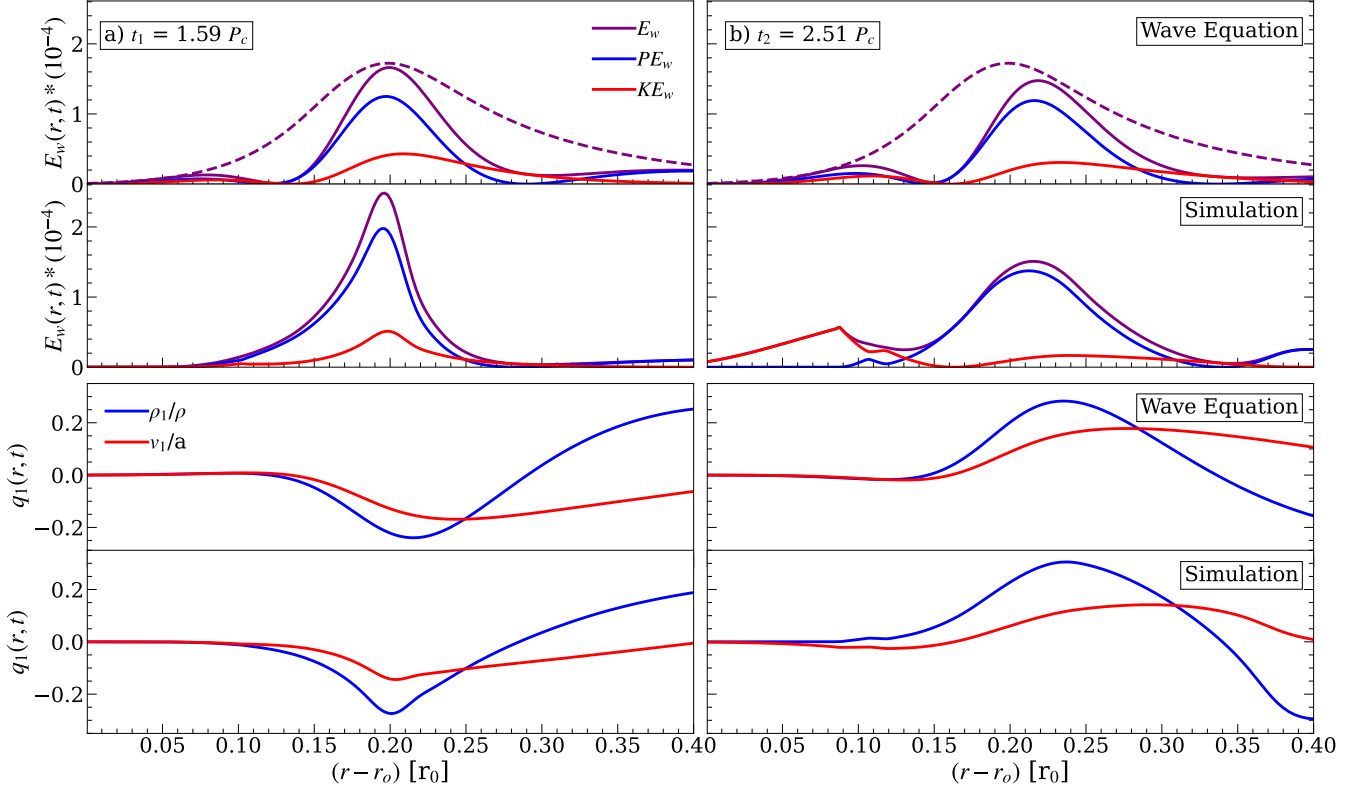


**Figure 5.** Comparison between the solution of the wave equation for a single-dominant frequency and the multi-frequency wave obtained from the time-dependent simulation (see the legends in the top left corner of the panels in the right column). The top two panels show radial profiles of  $E_w$  and its potential ( $PE_w$ ) and kinetic ( $KE_w$ ) components, the purple, blue, and red curves, respectively (see eq. 11). The multi-frequency behavior of the time-dependent simulation is illustrated in Fig. 2. The bottom two panels show corresponding density and velocity perturbation profiles, blue and red curves, respectively. The panels in the left column correspond to the time  $t_1 = 1.59 P_c$  where the wind starts its periodic cycle. The panels in the right column show a specific snapshot where the solution experiences a kink after a time  $\Delta t = 0.92 P_c$ . Both  $t_1$  and  $t_2$  are marked with the vertical dashed lines in the top panel of Fig. 2.

mass flux and the line force so that the flow undergoes repeated acceleration, deceleration, and collapse. The weakening of the line force due to ionization plays a significant role in the self-excitation behavior because the self-excitation behavior emerges as  $\delta$  increases. The wind solution exhibits characteristic kinks in the radial velocity profiles. Such kinks in line-driven winds are not a new phenomenon. For example, [Feldmeier et al. \(2008\)](#) studied the propagation of kink behavior by manually perturbing the density at the simulation lower boundary. In our work, the perturbations self-excite because the nearly static flow quickly decelerates to a collapsing solution that tends to re-accelerate. As the flow re-accelerates, the line force becomes insufficient again, and the cycle repeats.

The resulting fluctuations propagate into the solution and take on the characteristics of Abbott waves. The line force adds energy to the waves as they travel through the remaining exponential atmosphere. The added energy causes the density and velocity pertur-

bations to grow beyond what is expected by conserving wave energy flux, although the perturbations do not become fully non-linear.

In an exponentially stratified atmosphere, the perturbed velocity increases exponentially by conserving wave energy flux (e.g., [Clarke & Carswell 2007](#)). The exponential increase causes an intrinsic, proportional relationship between  $v_1$  and  $v'_1$ . The proportional relationship allows  $g_{l,1}$  to respond in phase with  $v_1$ , leading to the wave energy growth. In contrast with the results of a local analysis, where  $g_{l,1}$  responds  $90^\circ$  out of phase with the acoustic perturbations, yielding a stable wave ([Owoczi 2014](#)). As such, in our case, the wave energy growth we observe is in a non-WKB limit, i.e., the amplitude and phase change on a similar scale. The growth occurs dominantly for perturbations with the frequency close to  $\omega_c$  and is confined to the exponential atmosphere.

The appearance of energy growth is sensitive to the lower boundary conditions and  $\delta$ . The location of the

lower boundary and the density,  $\rho_0$ , there, sets the size of the stratified atmosphere captured by the simulations.

In particular, it determines whether the simulation includes or excludes the unsteady region. The stratification is set by  $\text{HEP}_0$ , with a large  $\text{HEP}_0$  indicating a colder, more stratified atmosphere. The line force weakening, parameterized by  $\delta$ , reduces the wind velocity and velocity gradient, leading to an increase of the Abbott speed that in turn leads to instability. The wave energy growth and self-excitation behaviors emerge as  $\delta$  is a significant fraction of the CAK  $\alpha$  parameter.

The instability could have significant implications for X-ray binaries (XRBs) and AGNs. In D24, they showed that, for the models with the XRB and AGN type SEDs,  $\delta$  can be as high as  $\alpha$ . Therefore, AGN winds could be intrinsically variable due to the weakening of the line force. This conjecture needs confirmation in 2D or 3D simulations similar to those performed by Proga et al. (2000); Kurosawa & Proga (2009); Dyda & Proga (2018); Dyda et al. (2024).

The self-excitation and instability, we identified, operate in the subsonic flow where the Sobolev approximation is formally invalid. This approximation and the CAK line-driven wind theory continues to be the basis of wind models because of its success in accounting for winds in OB stars (see, for example, Lamers & Cassinelli 1999) and its relatively low computational cost that makes 2D and 3D time-dependent simulations feasible. But it would be important to check how the lower boundary conditions affect the time behavior using non-Sobolev treatment of the line force such as full comoving-frame transfer (Pauldrach et al. 1986), smooth source function (Owocki 1991) or escape-integral source function (Owocki & Puls 1996). According to the CAK theory, the gross wind properties do not depend on the assumed density at the wind base. However, simulations of the line driven winds show that the solution could be variable if  $\rho_0$  is relatively high (e.g., Owocki et al. 1994; Proga 1999). For the time-dependent simulations to reproduce the stationary CAK wind solution, Proga (1999) adopted the following rule of thumb: set  $\rho_0$  large enough for the solution to be stationary but not too large that the solutions begins in the transonic region. Moving beyond the Sobolev approximation would also be essential in capturing additional physics of line-driven winds, especially line-deshadowing instability that operates on sub-Sobolev length scales (MacGregor et al. 1979; Carlberg 1980; Owocki & Rybicki 1984). Near the sub-surface of stars there may be acoustic instability due to radiative diffusion (e.g., der Sijpt et al. 2025, and references therein). In which case, as the acoustic wave propagates there may be parameter spaces where both

the Sobolev and non-Sobolev effects drive variability in the transition from the stellar atmosphere to the wind.

## ACKNOWLEDGMENTS

Support for this work was provided by the National Aeronautics and Space Administration under TCAN grant 80NSSC21K0496. I would also like to thank Shalini Ganguly and Sergei Dyda for fruitful discussions.

## APPENDIX

## A. DERIVATIONS

A.1. *Deriving Conservation of Acoustic Energy Equation*

We derived the wave energy conservation equation following a similar procedure as outlined by [Landau & Lifshitz \(1959\)](#) and [Mihalas & Weibel-Mihalas \(1999\)](#). By applying Eulerian perturbations to the mass continuity and momentum eq. 5 and 6, and using an isothermal equation of state, we obtain the perturbation equations

$$\frac{\partial \rho_1}{\partial t} = -\frac{1}{r^2} \frac{\partial}{\partial r} (r^2 (v \rho_1 + v_1 \rho)), \quad (\text{A1})$$

and

$$\rho \frac{\partial v_1}{\partial t} + \rho \frac{\partial (v_1 v)}{\partial r} + a^2 \left( \frac{\partial \rho_1}{\partial r} - \frac{\rho_1}{\rho} \frac{\partial \rho}{\partial r} \right) = \rho g_{l,1}. \quad (\text{A2})$$

By multiplying eq. A2 by  $v_1$  and eq. A1 by  $\frac{v_1}{\rho}$  and summing, we obtain

$$\frac{p_1}{\rho a^2} \frac{\partial p_1}{\partial t} + \rho v_1 \frac{\partial v_1}{\partial t} + v_1 \left( \frac{\partial p_1}{\partial r} - \frac{p_1}{\rho} \frac{\partial \rho}{\partial r} \right) = \rho v_1 g_{l,1} - \rho v_1 \frac{\partial (v_1 v)}{\partial r} - \frac{p_1}{\rho} \frac{1}{r^2} \frac{\partial}{\partial r} (r^2 (\rho_1 v + \rho v_1)). \quad (\text{A3})$$

We expand the last term on the right-hand side of eq. A3, cancel and regroup terms, yielding

$$\frac{p_1}{\rho a^2} \frac{\partial p_1}{\partial t} + \rho v_1 \frac{\partial v_1}{\partial t} + \frac{1}{r^2} \frac{\partial (r^2 p_1 v_1)}{\partial r} = -\rho v_1 \frac{\partial (v v_1)}{\partial r} - \frac{\rho_1}{\rho} \frac{1}{r^2} \frac{\partial (r^2 p_1 v)}{\partial r} + \rho v_1 g_{l,1}. \quad (\text{A4})$$

Considering  $v_1 \frac{\partial v_1}{\partial t} = \frac{1}{2} \frac{\partial (v_1^2)}{\partial t}$ , the first two terms in eq. A4 are rewritten in the form of the conservation of acoustic energy, eq. 10.

A.2. *Deriving Mass Flux Wave Equation*

By following the procedure detailed in [Petterson et al. \(1980\)](#) and using equation 12, we derive the mass flux wave equation. Specifically, we use eq. 15 and 12 to rewrite A1 and A2 as,

$$\frac{\partial \rho_1}{\partial t} = -\frac{1}{r^2} \frac{\partial f_1}{\partial r}, \quad (\text{A5})$$

and

$$\frac{\partial v_1}{\partial t} + \frac{\partial (v_1 v)}{\partial r} + \frac{a^2}{\rho} \left( \frac{\partial \rho_1}{\partial r} - \frac{\rho_1}{\rho} \frac{\partial \rho}{\partial r} \right) = 2v_a \left[ \left( \frac{\delta}{\alpha} - 1 \right) \frac{\rho_1}{\rho} v' + v_1' \right]. \quad (\text{A6})$$

We multiply eq. A6 by  $r^2 \rho$  and substitute the relationships,

$$\frac{1}{\rho} \frac{\partial \rho}{\partial r} = \frac{-v'}{v} - \frac{2}{r}, \quad (\text{A7})$$

and

$$r^2 \rho \frac{\partial v_1}{\partial t} = \frac{\partial f_1}{\partial t} + v \frac{\partial f_1}{\partial r} = \frac{df_1}{dt}, \quad (\text{A8})$$

which we obtained by using the property of mass continuity and the mass flux perturbation. The combined steps yield

$$\frac{\partial f_1}{\partial t} + v \frac{\partial f_1}{\partial r} + f \frac{\partial v_1}{\partial r} + v_1 r^2 \rho v' + a^2 \left[ r^2 \frac{\partial \rho_1}{\partial r} + r^2 \rho_1 \left( \frac{v'}{v} + \frac{2}{r} \right) \right] = 2v_a \left[ \left( \frac{\delta}{\alpha} - 1 \right) v' r^2 \rho_1 + r^2 \rho \frac{\partial v_1}{\partial r} \right]. \quad (\text{A9})$$

By taking the time derivative  $\frac{\partial}{\partial t}$  of A9, we get

$$\frac{\partial^2 f_1}{\partial t^2} + v \frac{\partial^2 f_1}{\partial r \partial t} + f \frac{\partial^2 v_1}{\partial r \partial t} + \frac{\partial v_1}{\partial t} r^2 \rho v' + a^2 \left[ r^2 \frac{\partial \rho_1}{\partial r \partial t} + r^2 \frac{\partial \rho_1}{\partial t} \left( \frac{v'}{v} + \frac{2}{r} \right) \right] = 2v_a \left[ \left( \frac{\delta}{\alpha} - 1 \right) v' r^2 \frac{\partial \rho_1}{\partial t} + r^2 \rho \frac{\partial v_1}{\partial r \partial t} \right]. \quad (\text{A10})$$

Finally, we use eq. A5 to replace the  $\frac{\partial \rho_1}{\partial t}$  terms and the relation A8 to replace the  $\frac{\partial v_1}{\partial t}$  terms. After canceling the appropriate terms, we will arrive at eq. 14 for the mass flux wave equation in an isothermal line-driven wind.

### A.3. Local Analysis of the Conservation of Energy Equation

Local analysis of the three terms on the RHS of eq. 10 suggests that the line force, divergence, and wave-flow interaction should remove specific energy from the wave (Key et al., submitted). For the average contribution of an acoustic cycle, the RHS of eq. 10 gives the terms

$$-\left\langle \rho v_1 \frac{\partial(vv_1)}{\partial r} \right\rangle = -\rho v' \langle v_1^2 \rangle - \rho v \left\langle v_1 \frac{\partial v_1}{\partial r} \right\rangle, \quad (\text{A11})$$

$$-\left\langle \frac{\rho_1}{\rho} \frac{1}{r^2} \frac{\partial(r^2 p_1 v)}{\partial r} \right\rangle = -\frac{2va^2}{\rho r} \langle \rho_1^2 \rangle - \frac{va^2}{r} \left\langle \rho_1 \frac{\partial \rho_1}{\partial r} \right\rangle - \frac{a^2}{\rho} v' \langle \rho_1^2 \rangle, \quad (\text{A12})$$

and

$$\langle \rho v_1 g_{l,1} \rangle = g_l (\delta - \alpha) \langle \rho_1 v_1 \rangle + \frac{\rho g_l}{v'} \left\langle v_1 \frac{\partial v_1}{\partial r} \right\rangle. \quad (\text{A13})$$

Considering a local oscillatory perturbation  $q_1 \propto \exp(i(kx - wt))$ , quantities of the form  $\langle q_1^2 \rangle$  and  $\langle q_1 \frac{\partial q_1}{\partial r} \rangle$  average to a positive value and zero, respectively. The term  $\langle \rho_1 v_1 \rangle$  would average to a positive value for velocity and density perturbations nearly in phase. Additionally, the quantities  $v', a, v, \rho, r$  are positive for a steady outflow and  $\alpha > \delta$  for all cases we investigated. Collectively, this suggests the average contribution of all terms on the RHS eq. 10 is negative. We would expect the line force to remove energy from the wave.

## REFERENCES

- Abbott, D. C. 1980, *Astrophysical Journal*, Part 1, vol. 242, Dec. 15, 1980, p. 1183-1207., 242, 1183
- Abbott, D. C. 1982, *ApJ*, 259, 282, doi: [10.1086/160166](https://doi.org/10.1086/160166)
- Arav, N., & Li, Z.-Y. 1994, *ApJ*, 427, 700, doi: [10.1086/174177](https://doi.org/10.1086/174177)
- Carlberg, R. 1980, *Astrophysical Journal*, Part 1, vol. 241, Nov. 1, 1980, p. 1131-1140. Research supported by the National Research Council of Canada., 241, 1131
- Castor, J. I., Abbott, D. C., & Klein, R. I. 1975, *ApJ*, 195, 157, doi: [10.1086/153315](https://doi.org/10.1086/153315)
- Clarke, C., & Carswell, B. 2007, *Principles of astrophysical fluid dynamics* (Cambridge University Press)
- Curé, M., & Araya, I. 2023, *Galaxies*, 11, 68
- Curé, M., Cidale, L., & Granada, A. 2011, *The Astrophysical Journal*, 737, 18, doi: [10.1088/0004-637X/737/1/18](https://doi.org/10.1088/0004-637X/737/1/18)
- Dannen, R., Proga, D., Waters, T., & Dyda, S. 2024, *The Astrophysical Journal*, 961, 221, doi: [10.3847/1538-4357/ad0da5](https://doi.org/10.3847/1538-4357/ad0da5)
- Dannen, R. C., Proga, D., Kallman, T. R., & Waters, T. 2019, *ApJ*, 882, 99, doi: [10.3847/1538-4357/ab340b](https://doi.org/10.3847/1538-4357/ab340b)
- Dannen, R. C., Proga, D., Waters, T., & Dyda, S. 2020, *ApJL*, 893, L34, doi: [10.3847/2041-8213/ab87a5](https://doi.org/10.3847/2041-8213/ab87a5)
- der Sijpt, C. V., Sundqvist, J., Debnath, D., Driessen, F., & Moens, N. 2025. <https://arxiv.org/abs/2501.09378>
- Dyda, S., Dannen, R., Waters, T., & Proga, D. 2017, *MNRAS*, 467, 4161, doi: [10.1093/mnras/stx406](https://doi.org/10.1093/mnras/stx406)
- Dyda, S., Davis, S. W., & Proga, D. 2024, *MNRAS*, 530, 5143, doi: [10.1093/mnras/stae1159](https://doi.org/10.1093/mnras/stae1159)
- Dyda, S., & Proga, D. 2018, *MNRAS*, 478, 5006, doi: [10.1093/mnras/sty1257](https://doi.org/10.1093/mnras/sty1257)
- Feldmeier, A., Rätzel, D., & Owocki, S. 2008, *The Astrophysical Journal*, 679, 704
- Grappin, R., Cavillier, E., & Velli, M. 1997, *Astronomy and Astrophysics*, v. 322, p. 659-670, 322, 659
- Higginbottom, N., Proga, D., Knigge, C., et al. 2014, *ApJ*, 789, 19, doi: [10.1088/0004-637X/789/1/19](https://doi.org/10.1088/0004-637X/789/1/19)
- Horace, L. 1909, *Proceedings of the London Mathematical Society*, 2, 122
- Kallman, T., & Bautista, M. 2001, *ApJS*, 133, 221, doi: [10.1086/319184](https://doi.org/10.1086/319184)
- Kudritzki, R. P. 2002, *The Astrophysical Journal*, 577, 389
- Kurosawa, R., & Proga, D. 2009, *ApJ*, 693, 1929, doi: [10.1088/0004-637X/693/2/1929](https://doi.org/10.1088/0004-637X/693/2/1929)
- Lamers, H. J. G. L. M., & Cassinelli, J. P. 1999, *Introduction to Stellar Winds*
- Landau, L. D., & Lifshitz, E. M. 1959, *Fluid mechanics*
- MacGregor, K. B., Hartmann, L., & Raymond, J. C. 1979, *ApJ*, 231, 514, doi: [10.1086/157213](https://doi.org/10.1086/157213)
- Mihalas, D., & Weibel-Mihalas, B. 1999, *Foundations of radiation hydrodynamics* (Courier Corporation)
- Murray, N., Chiang, J., Grossman, S. A., & Voit, G. M. 1995, *ApJ*, 451, 498, doi: [10.1086/176238](https://doi.org/10.1086/176238)
- Mushotzky, R. F., Solomon, P. M., & Strittmatter, P. A. 1972, *ApJ*, 174, 7, doi: [10.1086/151463](https://doi.org/10.1086/151463)
- Owocki, S. 2014, arXiv preprint arXiv:1409.2084
- . 2020, *Proceedings of the International Astronomical Union*, 16, 1



- Owocki, S. P. 1991, in NATO Advanced Study Institute (ASI) Series C, Vol. 341, *Stellar Atmospheres - Beyond Classical Models*, ed. L. Crivellari, I. Hubeny, & D. G. Hummer, 235
- Owocki, S. P. 2018, in 3rd BRITE Science Conference, ed. G. A. Wade, D. Baade, J. A. Guzik, & R. Smolec, Vol. 8, 48–56
- Owocki, S. P., Cranmer, S. R., & Blondin, J. M. 1994, *ApJ*, 424, 887, doi: [10.1086/173938](https://doi.org/10.1086/173938)
- Owocki, S. P., & Puls, J. 1996, *ApJ*, 462, 894, doi: [10.1086/177203](https://doi.org/10.1086/177203)
- Owocki, S. P., & Rybicki, G. B. 1984, *ApJ*, 284, 337, doi: [10.1086/162412](https://doi.org/10.1086/162412)
- Pauldrach, A., Puls, J., & Kudritzki, R. P. 1986, *A&A*, 164, 86
- Petterson, J. A., Silk, J., & Ostriker, J. P. 1980, *MNRAS*, 191, 571, doi: [10.1093/mnras/191.3.571](https://doi.org/10.1093/mnras/191.3.571)
- Proga, D. 1999, *MNRAS*, 304, 938, doi: [10.1046/j.1365-8711.1999.02408.x](https://doi.org/10.1046/j.1365-8711.1999.02408.x)
- Proga, D. 2005, in *Astronomical Society of the Pacific Conference Series*, Vol. 330, *The Astrophysics of Cataclysmic Variables and Related Objects*, ed. J. M. Hameury & J. P. Lasota, 103
- Proga, D. 2007, in *Astronomical Society of the Pacific Conference Series*, Vol. 373, *The Central Engine of Active Galactic Nuclei*, ed. L. C. Ho & J. W. Wang, 267
- Proga, D., Stone, J. M., & Kallman, T. R. 2000, *ApJ*, 543, 686, doi: [10.1086/317154](https://doi.org/10.1086/317154)
- Puls, J., Springmann, U., & Lennon, M. 2000, *Astron. Astrophys. Suppl. Ser.*, 141, 23, doi: [10.1051/aas:2000312](https://doi.org/10.1051/aas:2000312)
- Sim, S. A., Proga, D., Miller, L., Long, K. S., & Turner, T. J. 2010, *MNRAS*, 408, 1396, doi: [10.1111/j.1365-2966.2010.17215.x](https://doi.org/10.1111/j.1365-2966.2010.17215.x)
- Stone, J. M., Tomida, K., White, C. J., & Felker, K. G. 2020, *ApJS*, 249, 4, doi: [10.3847/1538-4365/ab929b](https://doi.org/10.3847/1538-4365/ab929b)